Optical Engineering

SPIEDigitalLibrary.org/oe

Empirical modeling for non-Lambertian reflectance based on full-waveform laser detection

Xiaolu Li
Lian Ma
Lijun Xu

SPIE

Empirical modeling for non-Lambertian reflectance based on full-waveform laser detection

Xiaolu Li
Lian Ma
Lijun Xu
Beihang University
School of Instrument Science and Opto-Electronic Engineering
Beijing 100191, China
E-mail: lijunxu@buaa.edu.cn

Abstract. Empirical models are proposed for recalculating non-Lambertian reflectance based on the transmitted pulses and returned pulses that are recorded by a lab-built full-waveform laser detection system. The experiments were implemented on three objects, which were gray-cement concrete, red dull paper, and glazed indoor tile. The pulse energy was calculated based on the pulse waveforms in two ways, integral of the waveform (IW) method and multiplying peak by the full width at half maximum of the waveform (PF) method. The newly introduced empirical parameters semi-ellipsoid distribution ratio (SEDR) of the semi-ellipsoid model and ellipsoid distribution ratio (EDR) of the ellipsoid model were put forward to evaluate the degree of the non-Lambertian reflectance of material surface, instead of Lambertian-based factor that is the cosine of the incidence angle. We conclude that the bigger values of SEDR and EDR indicate more significant deviation from Lambertian for material surface. The modified reflectance results estimated by using the semi-ellipsoid model display better approximations than those obtained from Phong cosine. Moreover, it is obvious that the modified reflectance using a combined method of PF and modified semi-ellipsoid model outweighs the results estimated by other manners.
[DOI: 10.1117/1.OE.52.11.116110]

Subject terms: reflectance; non-Lambertian; empirical model; full-waveform laser detection.

Paper 131359 received Sep. 6, 2013; revised manuscript received Oct. 27, 2013; accepted for publication Oct. 30, 2013; published online Nov. 20, 2013.

1 Introduction

The characterization of reflective properties of materials can be realized by defining the function that determines how reflected radiance is distributed in terms of the distribution of incident radiance. This function is the bidirectional reflectance distribution function (BRDF).[1] BRDF as a model is useful for different kinds of reflection descriptions and depends only on the characteristics of the material surface. The completely diffuse bihemispherical albedo can be derived through integration of the BRDF for the entire solar and viewing hemisphere,[2] while the direct beam directional hemispherical albedo can be calculated through integration of the BRDF for a particular illumination geometry.[3] To estimate remotely sensed albedo, reflectance measurements must be interpreted with the help of BRDF models for retrieving the required variables from the actual observations. In general, BRDF models can be classified into one or two of these categories: theoretical model (physical-based model), data-driven model, and empirical model (phenomenological model). Theoretical models try to accurately explain light scattering by using physics laws. The typical theoretical model was the microfacet model, which was the basis for the individual models such as Torrance-Sparrow BRDF,[4,5] Cook-Torrance,[6] Oren-Nayar BRDF,[7] and so on. They usually lead to complex expressions and high computational effort. These theoretical models result in a very difficult nonlinear optimization problem; thus they are not normally employed in rendering systems. In contrast, data-driven techniques use the measured data for rendering, which describe reflectance directly based from the tabulated data. However, the classical data-driven techniques, like tensor factorization, are not well suited for data sets as they require a resampling of the high-dimensional measurement data to a regular grid. It interpolates and extrapolates new BRDF models from the representative BRDF data.[8] The aim of the empirical model is to provide a simple expression that can be fast computationally and adjustable by parameters,[1] but the empirical models approximate the reflectance without analyzing the underlying principles of physics. It is often used to generate *ad hoc* empirical formulas attempting to reproduce the typical reflectance properties seen in real surfaces. One of the first empirical models in terms of an exponent parameter responsible for darkening was advanced by Minnaert to model the lunar surface reflectance.[9] Phong is still a very popular BRDF model, and it was the first description for a non-Lambertian surface, which is an empirical model according to its simplicity. This has made it one of the most used empirical models in light reflection description.[10] However, Phong models are not appropriate for many objects when the experiments were implemented on laser detection systems. In this paper, an empirical model with new parameters was put forward to calculate the reflectance in terms of the distribution of incident radiance.

A diffuse surface complies with the BRDF that has the same reflective intensity values for all incident and outgoing directions. This substantially reduces the computations and thus it is commonly used to model diffuse surfaces as it is physically plausible, even though there are no pure diffuse materials in the real world. For diffuse reflection, the light is reflected on a tarnished surface. Its intensity follows the

Lambert's cosine law.[11] According to the cosine law, the intensity of diffuse reflection light is proportional to the cosine of the angle between the incidence light and the surface normal to the target to the lowest order. Furthermore, the intensity is inversely proportional to the square of the distance between the target and the observation. However, most objects are not tarnished and cannot be considered as Lambertian surfaces in practice. As far as we know, some methods were reported to obtain the absolute reflectance of different targets based on the extracted intensity.[12] Generally speaking, objects with high reflectance, such as snow or a metal roof, show a higher reflected intensity than dark objects, such as the asphalt roadway.[13] Höfle has summarized two different methods, data-driven correction and model-driven correction, to correct the intensity data for the influences resulting in a value proportional to the reflectance of the scanned surface.[14] Then Wagner indicated that the pulse waveforms provide important information about the reflectance of the observed targets, geophysical parameter retrieval, and advanced geometric modeling.[15] Except for intensity extraction from the waveforms, Paul introduced a method of using the number of photons returned to each detector to calculate the received power; then the reflectance of the targets can be deduced.[16] Besides these reflectance measurement methods based on intensity calculation, Wei proposed a means of target surface reflectance measurement by measuring incidence energy, laser spot size, and reflection energy directly.[17] In addition to intensity values, incident angle and measuring distance are also crucial information for reflectance calculation. For example, angle-resolved scattering techniques have to deal with issues of changing area of illumination with incident angle, which varies according to the cosine of the incident angle of the lowest order, and possible shadowing and multiple scattering effects at large incidence angles.[18] In this study, the reflected pulse energy of the objects is calculated based on their returned full-waveforms, and the laser detection experiments are designed and implemented with variational incident angles and detection distances.

Recently most state-of-the-art full-waveform laser detection systems record the intensity of the returned pulse in addition to recording the time of a returned pulse. That is, they not only measure the fact that there is a returned pulse, but also measure the intensity of the full returned echoes. The new technology of full-waveform laser detection systems permits us to record the complete waveforms of the backscattered pulses.[19] Besides, a series of new experimental full-waveform laser detection systems have been developed by scientists, and the measurements have been carried out. In 2003, Jutzi constructed an experimental system to record the returned signals of targets based on which different urban materials could be distinguished. However, the minimum recording time was 1 ms per measurement of the returned waveform.[20] In addition, Kirchhof utilized a full-waveform laser detection system to obtain three-dimensional points of the surface. However, in this system the laser had a pulse duration of 5 ns at full-width-at-half-maximum (FWHM) and the bandwidth of the detector was only 250 MHz. The temporal resolution would be low because of the short pulse duration and the narrow bandwidth of the detector.[21] In order to improve the sampling frequency, the bandwidth of the detector, and the pulse duration, an experimental laser detection system with a sampling frequency of 1 GHz was set up in our laboratory for measuring the reflectance of three different targets in this study. The energy of the returned waveforms of these three targets was calculated based on the data collected by the laser detection system, which has a 1064-nm laser transmitter with a pulse duration of 6 ns at FWHM. Moreover, the sampling time can be long enough, thanks to the large storage capacity of the laser detection system.

The remainder of this paper is organized as follows. In Sec. 2, the setup of the full-waveform laser detection system was introduced and the data acquisition mode was described; then Lambertian-based light scattering theory of laser detection was elaborated. In Sec. 3, the energy estimations of returned waveforms were processed in two ways [integral of waveform (IW) method and pulse peak multiplying by FWHM (PF) method]. Then, the novel empirical parameters are proposed to evaluate the degree of the non-Lambertian reflectance of materials in Sec. 4. The concluding remarks are given in Sec. 5.

2 Setup and Methodology

2.1 *Setup*

The purpose of the setup of the full-waveform laser detection system is to record the transmitted pulses and the returned waveforms for measuring the reflectance of different objects in this study. The laser pulse was transmitted from a 1064-nm laser on the opposite side of the target. Laser controllable repetition rate can be controlled from 1 Hz to 5 kHz, and the average power of the laser is 83 mW at a 5 kHz repetition rate. The light scattered from the sample is received by the focusing lens and part of it is detected by a PIN photodetector. Specific characteristics of optical devices mentioned above are shown in Table 1. The detected pulses were recorded by the data acquisition system. The data acquisition system includes a data acquisition card and a control unit, both of which are constructed by National Instruments (NI), Austin, TX. NI5751R was used as the control unit, which includes a reconfigurable field-programmable gate array module and an adapter module. The control unit, which can be programmed by Labview software, triggers the digitizer and the laser transmitter to collect data and transmit pulses, respectively. The PXI-5154 high-speed digitizer with 8 Mb onboard memory is used as the data acquisition card. It can be programmed by Labview software to set the acquisition mode and has a maximum real-time sampling frequency of 1 GHz. Both the PXI-5154 digitizer and NI5157R are plugged into the Pxle-1082 eight-slot chassis constructed by NI as well.

The PXI-5154 high-speed digitizer has three channels, two of them (CH0 and CH1) can not only be selected as a data acquisition channel, but also be used as a trigger channel. The remaining one (TRIG) can only be used as a trigger channel. In this study, CH0 was the data acquisition channel and CH1 was the trigger channel. Before the step of data acquisition, PXI-5154 should be initialized by the driver, and then parameters such as sampling rate, amplitude range, and trigger mode need to be set. The 1 GHz sampling rate was set to meet the requirement for reducing distortion of the collected signal. Therefore, the laser transmitted pulses and the received waveforms were sampled at 1-ns intervals with 8-bits amplitude resolution. The amplitude range was set

Table 1 Characteristics of the experimental optical devices.

Laser wavelength	1064 nm
Laser energy/per pulse	16.6 μJ
Pulse duration (FWHM)	6 ns
Average power	83 mW
Beam divergence	1.5 mrad
Transverse mode	TEM_{00}
Pulse repetition frequency	1 to 5 kHz
Focal length	77 mm
Diameter of focusing lens	35 mm
Detector diameter	10 mm
Detector bandwidth	4 GHz
Quantum efficiency at peak	80%
Detector rise time	<70 ps

according to the intensity value of the returned waveforms detected by the PIN photodetector. The waveform data were collected by PXI-5154 using edge-triggered mode. When NI5751R sent a trigger pulse into CH1, PXI-5154 started to collect data and the transmitted pulse or the returned waveform data were collected through CH0 and stored in binary format.

2.2 *Light Scattering Theory*

The received energy of the laser detection system is mainly affected by four essential factors: instrumental and atmospheric effects, the target scattering characteristics, and the measurement geometry.[13] The radar equation summarizes all the parameters relevant to these effects on power of the backscattered signal collected by the detector. The specific Lambertian reflectance formulas based on radar equation are derived here, which provide the basis for further consideration. The laser transmits a narrow beam that has a divergence angle of θ_T toward the target. The footprint area of the beam at the target is approximately written as[22]

$$A_l = \frac{\pi R'^2 \theta_T^2}{4}, \tag{1}$$

where R' is the range from target to laser transmitter. The power density S_s of the laser beam at the footprint area is

$$S_s = \frac{4P_T}{\pi R'^2 \theta_T^2}, \tag{2}$$

where P_T is the transmitted power. The scattered light is reradiated by the effective area A_S in various directions; thus the scattered power P_s is

$$P_s = \frac{4P_T}{\pi R'^2 \theta_T^2} \rho A_S, \tag{3}$$

where ρ is the target reflectance. The reradiation pattern is, in general, complex, but for simplicity, the incoming radiation is assumed to be scattered uniformly into a cone of solid angle Ω. The power density S_r at the receiver is

$$S_r = \frac{4P_T}{\pi R'^2 \theta_T^2} \rho A_S \frac{1}{\Omega R^2}. \tag{4}$$

R is the range from the target to the receiver. The power entering the receiver with aperture diameter of D is

$$P_R = \frac{4P_T}{\pi R'^2 \theta_T^2} \rho A_S \frac{1}{\Omega R^2} \frac{\pi D^2}{4}. \tag{5}$$

Assuming that the entire footprint is a Lambertian surface and the incident angle α is greater than zero ($\alpha > 0$ deg), the effective area has a proportionality of cos α; thus the effective scattered area is[14]

$$A_s = \frac{\pi R'^2 \theta_T^2 \cos \alpha}{4}. \tag{6}$$

Furthermore, if the surface has Lambertian scattering characteristics, then Ω can be set as π. Substituting Eq. (6) into Eq. (5), we can obtain

$$P_R = \frac{P_T D^2 \rho \cos \alpha}{4R^2}. \tag{7}$$

Lambertian is a description of scattering and reemission of light from the body of a surface. Some of the ray is reflected at the surface into the detector, and the rest passes through the surface into the body of the object. In the process of transmission and detection of the reflected light, the laser pulse energy would be lost. Thus, taking the atmospheric transmission factor η_{atm} and system factor η_{sys} into consideration, the received energy can be revised as

$$P_R = \frac{P_T D^2 \eta_{\text{atm}} \eta_{\text{sys}} \rho \cos \alpha}{4R^2}. \tag{8}$$

Finally, the target reflectance ρ can be deduced as

$$\rho = \frac{4R^2}{D^2 \eta_{\text{atm}} \eta_{\text{sys}} \cos \alpha} \cdot \frac{P_R}{P_T}. \tag{9}$$

The atmosphere transmission factor η_{atm} can be neglected in our experiments since the transmission of laser pulse is within the optical table in a few meters distance. In this paper, the detecting and sampling system factor η_{sys} was 0.95, measured by the light power meter. The aperture diameter D of the focusing lens is 35 mm. The detail of parameters R and α recorded in the experiments will be described in Sec. 3.1. The two methods for calculating P_R and P_T from waveforms will be introduced in Sec. 3.2.

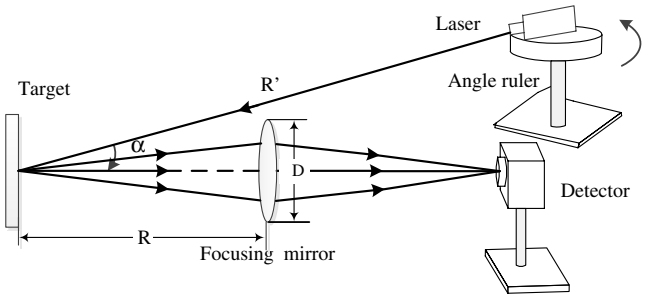

Fig. 1 Optical path illustration for collecting echoes.

3 Experiment and Results

3.1 *Experiment Procedure*

In order to research the reflectance of different materials, three kinds of objects, gray-cement concrete, red dull paper, and glazed indoor tile, are selected to carry out experiments to collect the returned waveforms at different ranges R and incident angles α. The optical path illustration of the laser detection system is shown in Fig. 1. The 1064-nm YAG laser is placed on a rotator, which is also an angle ruler for the purpose of adjusting the incidence angle. The laser pulses hit the targets, and then the light scattered from the targets passes through the focusing lens and part of it is detected by the PIN photodetector which is positioned at the focal point of the scattered light. Then the detected light is converted into electrical signals by the PIN photodetector and finally collected by the data acquisition system. To collect the returned waveforms of these three targets at different ranges R and incident angles α, multigroup experiments were carried out and the experiment results were recorded. First, the distance between target and focusing lens was fixed, and the rotator angle between the incident laser beam and the surface normal of the target was changed from 15 to 75 deg with a step of 15 deg. Then the distance between target and focusing lens was adjusted from 100 to 500 mm with a step length of 100 mm. At each fixed distance, the rotator angle was changed from 15 to 75 deg. Thus, at least 75 groups of experimental results for a certain material were saved to investigate the fundamental physics of the light scattered from materials.

3.2 *Two Energy Calculation Methods and Results*

The waveforms are collected and saved for calculating the energy of the transmitted and returned pulses after Gauss filtering. The typical demonstrations of raw echo waveforms and the filtered echo waveforms obtained in groups of experiments are shown in Fig. 2. The gray curves denote the raw waveforms, while the black ones represent the filtered waveforms. Three subplots of gray-cement concrete, red dull paper, and gray indoor tile all denote three raw echo waveforms and the corresponding filtered echo waveforms collected at an incidence angle of 15 deg and at a detection distances of 100, 200, and 300 mm, respectively. The filtered waveforms will be used to calculate the energy of the transmitted pulse and returned waveforms in two ways, described as follows.

3.2.1 *Method 1: Integral of waveform*

The photodetector converts optical power of the detected scattered light into electrical signals, and the conversion coefficient is a constant within the working range, which is defined as K. Hence, the energy is calculated by integrating the transmitted waveform or the returned waveform. This energy calculation method was referred to as the IW method. We can deduce the reflectance as

$$\rho = \frac{4R^2}{D^2\eta_{\text{atm}}\eta_{\text{sys}}\cos\alpha} \cdot \frac{\int_{t_1}^{t_2} f'_R(t)\mathrm{d}t}{\int_{t_1}^{t'_2} f'_T(t)\mathrm{d}t}, \tag{10}$$

where t_1 and t_2 are the beginning and end of relative time of the waveform. $f'_R(t)$ is the filtered returned waveform and $f'_T(t)$ is the filtered transmitted waveform.

3.2.2 *Method 2: Pulse peak multiplying by FWHM*

Although the returned and the transmitted waveforms were filtered by Gaussian filter, it is not easy to completely eliminate the noise. If the signal has low intensity relative to noise, the energy estimated by IW method would be blurred. Average power of the returned and the transmitted waveforms can be closely estimated by multiplying the pulse peak intensity with the FWHM to its interval. This method was referred to as the PF method, and the reflectance ρ is rewritten as

$$\rho = \frac{4R^2}{D^2\eta_{\text{atm}}\eta_{\text{sys}}\cos\alpha} \cdot \frac{I_R\omega_R}{I_T\omega_T}, \tag{11}$$

where I_R and I_T are the pulse peak intensity of the filtered returned and transmitted waveforms, respectively; ω_R and

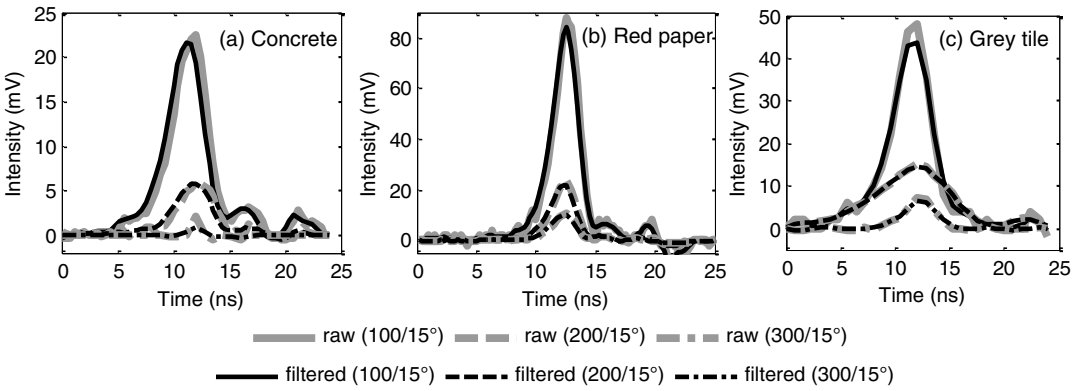

Fig. 2 Reflected raw waveforms and filtered waveforms of three targets.

ω_T are FWHM of the filtered returned and transmitted waveform, respectively.

3.3 *Relationship of R^2P_R and Reflectance*

The energy values of the returned waveforms of these three targets at different ranges and incident angles have also been calculated using IW and PF methods, respectively. Figure 3 plots the straightforward relationship between the returned energy P_R and the detection distance R, which shows a roughly inverse square law when the incident angle is fixed. It indicates that the received waveforms are credible because the relationships are in conformity with the conclusion reported by other researchers. However, the lines are not strictly straight lines as shown in Fig. 3, which may have resulted from the measured deviation in the experiment or the calculation error caused by the waveform noise which has not been eliminated. The average values of R^2P_R for gray-cement concrete, red dull paper, and glazed indoor tile using IW method are estimated as 0.0026 ± 0.0003, 0.0079 ± 0.0019, and 0.0040 ± 0.0011, respectively. Likewise, they are calculated to be 0.0020 ± 0.0002, 0.0068 ± 0.0015, and 0.0034 ± 0.0008 using the PF method. Further, it indicates that the received waveforms and the calculated energy are credible. When the incident angles are changed from 15 to 75 deg at a step of 15 deg, the average values of R^2P_R estimated for gray-cement concrete using IW method are 0.0026, 0.0020, 0.0026, 0.0027, and 0.0029, respectively. It is to be noted that the values of R^2P_R are not in direct proportion to the cosine of the angle for the three tested targets whether the IW method or PF method is adopted. Even so, the values of R^2P_R can also represent the energy reflectance ability of different materials. As mentioned above, the deduction based on Lambertian theory seems to not follow the physical law because most material surfaces do not have Lambertian behavior. Thus, it is necessary for us to put forward some models based on non-Lambertian for these three targets.

4 Modified Empirical Models

4.1 *Empirical Models*

The Lambertian-based scattering light theory shows that the apparent brightness of the target remains the same for all viewing angles. And the surface is called Lambertian when the body reflection obeys Lambert's cosine law, i.e., the intensity is directly proportional to the cosine of the angle from which it is viewed. This results in a radiation pattern that resembles a sphere. The ideal Lambertian target has the highest and most constant diffuse reflectance. In order to get the real reflectance distribution, the distribution ratio cos α was replaced by $\kappa(\alpha)$ and the reflectance is deduced as

$$\rho = \frac{C(\alpha)}{\kappa(\alpha)}. \tag{12}$$

According to Eq. (9), $C(\alpha)$ is

$$C(\alpha) = \frac{4R^2P_R(\alpha)}{D^2\eta_{\text{atm}}\eta_{\text{sys}}P_T}. \tag{13}$$

$C(\alpha)$ estimated for different targets is varied with incident angle α, as shown by data labeled with ◇ in Fig. 4. For subplots of Figs. 4(a), 4(b), and 4(c), the received pulse energies were calculated by the IW method, and for subplots of Figs. 4(d), 4(e), and 4(f), the received pulse energies were calculated by the PF method. At the same incidence angle, the data labeled with ◇ in the vertical direction of Fig. 4 shows the variations due to two reasons. One is that values of $R^2P_R(\alpha)$ were measured at different detection distances, which results in the measurement errors. The other one is that the values of $C(\alpha)$ in terms of P_R were estimated from two methods, IW and PF, which generated the calculation errors. It should be noted that the values of $C(\alpha)$ calculated from PF method at the same incidence appear more plausible than those calculated from the IW method, which

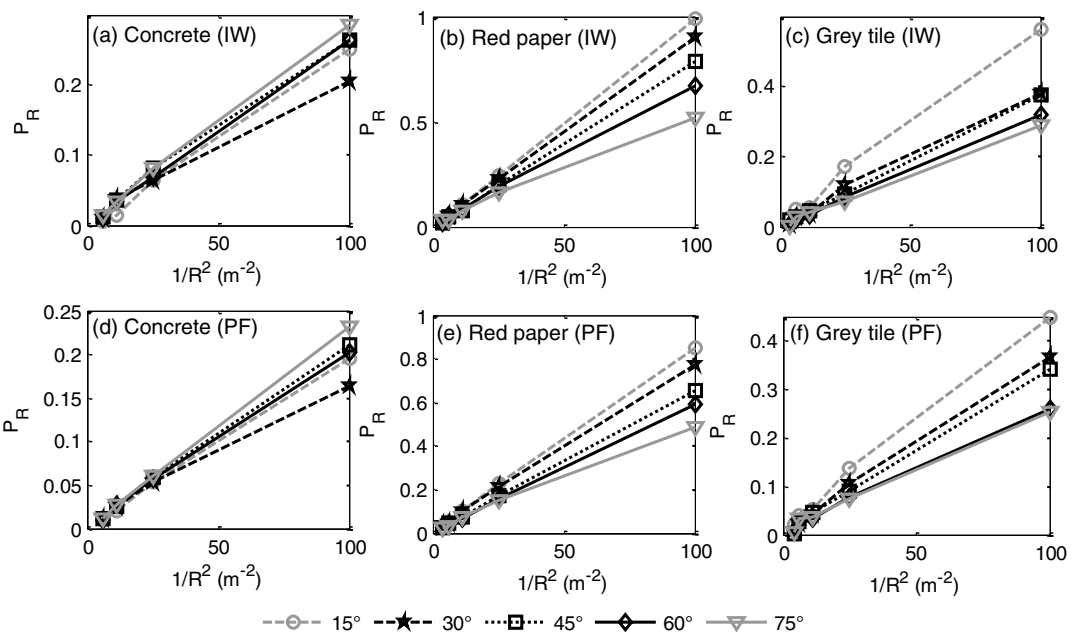

Fig. 3 The relationship of energy of returned pulse and inverse of square-R of three targets.

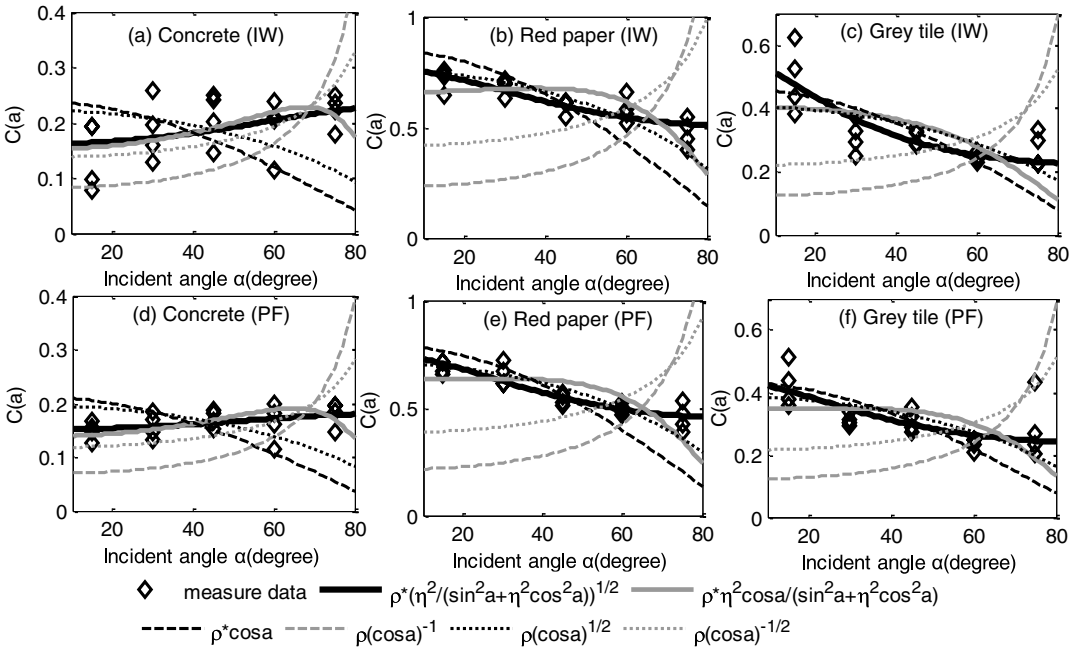

Fig. 4 Curve fitting for $C(\alpha)$ by the ellipsoid, semi-ellipsoid model, and multiorder cosine α. Black solid lines represent the curve fitting using semi-ellipsoid model and gray solid lines represent the curve fitting using ellipsoid model.

proved that PF method can reduce noise to a minimum, especially for signal in a low-SNR environment. Another point of view is that even though the values of $C(\alpha)$ of gray-cement concrete increase with the increase of incident angle, the values of $C(\alpha)$ of red dull paper and glazed indoor tile decrease with the increase of incidence angle. It leads to an intuitionistic phenomenon that various materials have different characteristics of scattering light when the incidence angles are adjusted. Therefore, the reflectance distribution ratio $\kappa(\alpha)$ related to the incidence angle must be reconsidered to describe material scattering light characteristics rather than being cos α only.

As we know, the statistical data analysis functions were used to acquire knowledge on measured values distribution in order to have an image based on accuracy and precision of measurements. After that, curve fitting algorithms were employed to find a function with minimal error, which complies with the measured data and can be a good candidate for calibration function. Here, we will present the obtained results of statistical analysis and curve fitting and the conclusions that can be drawn from these results. The values of $C(\alpha)$, calculated by both PF and IW methods, will employ different types of functions of $\rho\kappa(\alpha)$ for curve fitting. In order to rebuild the distribution ratio $\kappa(\alpha)$, the reflectance distribution was described by an ellipsoid model, a semi-ellipsoid model, and Phong's model as described below.

4.1.1 *Semi-ellipsoid model*

An ellipsoid with a long axis (z axis) of length 2b and two short axes (x and y axes) of length 2a, whose center locates at (0,0,0), is referred to as semi-ellipsoid model. Once the reflectance ratio ρ is a constant coefficient, the length of any point of the semi-ellipsoid regarded as reflectance distribution $C(\alpha)$ is written as

$$C(\alpha) = \rho_{\text{fse}} \sqrt{\frac{\eta_{\text{fse}}^2}{\sin^2\alpha + \eta_{\text{fse}}^2 \cos^2\alpha}}. \tag{14}$$

η_{fse} is the ratio of the short axis of the semi-ellipsoid to the long axis, that is, $\eta_{\text{fse}} = \text{a/b}$. ρ_{fse} is the reflectance estimated by fitting Eq. (14) to the measurement data of $C(\alpha)$. The fitting curves using Eq. (14) were shown as black solid lines in Fig. 4.

4.1.2 *Ellipsoid model*

A prolate ellipsoid with a long axis (z axis) of length 2b and two short axes (x and y axes) of length 2a, whose center locates at (0, 0, b), is referred to as ellipsoid model. The length of any point of an ellipsoid regarded as reflectance distribution $C(\alpha)$ is written as

$$C(\alpha) = \rho_{\text{fe}} \frac{\eta_{\text{fe}}^2 \cos\alpha}{\sin^2\alpha + \eta_{\text{fe}}^2 \cos^2\alpha}. \tag{15}$$

η_{fe} is the ratio of the short axis of the ellipse to the long axis, that is, $\eta_{\text{fe}} = a/b$. When $\eta_{\text{fe}} = 1$, $\kappa(\alpha) = \cos\alpha$; thus the ellipsoid becomes a sphere. Lambertian model is thought to be an extended example of the ellipsoid model. ρ_{fe} is the fitting reflectance estimated by Eq. (15). The fitting curves using Eq. (15) are shown as gray solid lines in Fig. 4.

4.1.3 *Phong's model*

Phong's model indicates that the amount of light perceived by the viewer depends on the angle between the outgoing light and the direction of the viewer and is proportional to $\cos^n\alpha$. The fitting curves were shown as the dotted lines and dashed lines with colors of black and gray in Fig. 4.

4.2 *Fitting Results*

In order to perform and analyze curve fitting, we define the functions mentioned above, which depend on the parameters in terms of the incident angle α and the fitting reflectance ρ. In this study, if the fitting functions of Phong models with different values of n are selected with a trend of monotonic growth or regression, the functions are obviously not suitable for all the targets at the same time. Just as the curve fitting with gray dashed line and dotted line for gray-cement concrete are increasing, the values of n of fitting functions are -1 or $-1/2$, while as the fitting curves with black dashed line and dotted line for red dull paper and glazed indoor tile are decreasing, the values of n are 1 or $1/2$, as shown in Fig. 4. When Eqs. (14) and (15) are used as the fitting functions, the fitting results are averagely credible as shown by the black and gray solid curves in Fig. 4. The root mean square of estimated residuals of the fitting curves for three materials are shown in Table 2. From Fig. 4 and Table 2, we can see that semi-ellipsoid model has a minimum fitting error followed by the ellipsoid model. It is evident that the semi-ellipsoid model and ellipsoid model are more suitable to describe reflectance distribution for these three targets than the Lambertian model ($\cos\alpha$) and those multiorder Phong cosine models ($\cos^n\alpha$). Likewise, as shown in Table 2, the estimated residuals calculated by the PF method were also less than those calculated by the IW method. From another point of view, it can prove that the energy calculated by the PF method can create the noise elimination effect.

As mentioned earlier, the parameter $\kappa(\alpha)$ relative to incidence angle is utilized to simulate the real material scattering light characteristic instead of being $\cos\alpha$ only. For ellipsoid model, the η_{fe}, called ellipsoid distribution ratio (EDR), is a ratio of the semiprincipal axes of x-axis length to z-axis length. For semi-ellipsoid model, η_{fse} is a ratio of the semiprincipal axes of x-axis length to z-axis length, which can be referred to as semi-ellipsoid distribution ratio (SEDR). The values of EDR and SEDR, which can be defined from zero to infinity, are different with the various targets. Thus, they can both be denoted as the empirical factors influenced by the scattering characteristics of materials and can be used for materials discrimination. As mentioned above, when $\eta_{\mathrm{fe}}=1$, the ellipsoid model becomes a sphere. Thus, when EDR η_{fe} was estimated >1, the greater values of EDR η_{fe} indicate that the distribution ratio $\kappa(\alpha)$ deviated more from a sphere, namely, the targets behave increasingly like a non-Lambertian. From Table 3, it can be seen that the values of EDR η_{fe} and SEDR η_{fse} have roughly equal ratios for these three targets based on both the IW method and the PF method. So we can see that the values of EDR η_{fe} and SEDR η_{fse} reveal a similar material characteristic of non-Lambertian scattering. Here, the bigger values of EDR and SEDR indicate that the surface is more non-Lambertian. The gray-cement concrete has the largest values of η_{fe} and η_{fse} to act as a target deviating from non-Lambertian mostly, which is consistent with the physical fact reported in Ref. 13. More specifically, for gray-cement concrete, red dull paper, and glazed indoor tile, the EDR η_{fe} are calculated by IW method to be 2.82, 1.62, and 1.25, respectively, and SEDR η_{fse} are calculated by IW method to be 1.42, 0.66, and 0.41, respectively. Except for the empirical factors, EDR η_{fse} and SEDR η_{fe}, the fitting reflectance ρ_{fse} and ρ_{fe} also vary with different targets, which are shown in the third and fourth rows of Table 3. We can see that the estimation values of fitting reflectance ρ_{fse} and ρ_{fe} are on a same scale for the three kinds of targets. The underlying relationship of the fitting reflectance and modified reflectance calculated from the modified formulas will be proved in the next part.

4.3 *Modified Reflectance*

4.3.1 *Reflectance results*

Based on the empirical factors of SEDR η_{fse} and EDR η_{fe}, the modified reflectance of the targets are rewritten as

$$\rho_{\mathrm{mse}}=\frac{4R^2}{D^2\eta_{\mathrm{atm}}\eta_{\mathrm{sys}}\sqrt{\frac{\eta_{\mathrm{fse}}^2}{\sin^2\alpha+\eta_{\mathrm{fse}}^2\cos^2\alpha}}}\times\frac{P_R}{P_T}, \tag{16}$$

$$\rho_{\mathrm{me}}=\frac{4R^2}{D^2\eta_{\mathrm{atm}}\eta_{\mathrm{sys}}\frac{\eta_{\mathrm{fe}}^2\cos\alpha}{\sin^2\alpha+\eta_{\mathrm{fe}}^2\cos^2\alpha}}\times\frac{P_R}{P_T}. \tag{17}$$

Table 2 The estimated residuals of fitting curves.

	Targets					
	Concrete		Paper		Tile	
	IW	PF	IW	PF	IW	PF
Models	RMS	RMS	RMS	RMS	RMS	RMS
$\rho\eta_{\mathrm{fse}}/(\sin^2\alpha+\eta_{\mathrm{fse}}^2\cos^2\alpha)^{1/2}$	0.05	0.02	0.05	0.04	0.06	0.06
$\rho\eta_{\mathrm{fe}}^2\cos\alpha/(\sin^2\alpha+\eta_{\mathrm{fe}}^2\cos^2\alpha)$	0.05	0.02	0.07	0.08	0.09	0.08
$\rho\cos\alpha$	0.10	0.07	0.15	0.13	0.10	0.10
$\rho(\cos\alpha)^{-1}$	0.08	0.07	0.37	0.34	0.22	0.19
$\rho(\cos\alpha)^{1/2}$	0.08	0.05	0.07	0.06	0.08	0.07
$\rho(\cos\alpha)^{-1/2}$	0.06	0.04	0.24	0.22	0.16	0.14

Table 3 Fitting coefficients and modified reflectance results for three targets.

	Targets					
	Concrete		Paper		Tile	
Parameter	IW	PF	IW	PF	IW	PF
η_{fse} (SEDR)	1.4226	1.2031	0.6601	0.6089	0.4091	0.5503
η_{fe} (EDR)	2.8220	2.5507	1.6215	1.5289	1.2543	1.5144
ρ_{fse} (fitting reflectance)	0.1609	0.1506	0.7641	0.7438	0.5469	0.4345
ρ_{fe} (fitting reflectance)	0.1511	0.1376	0.6565	0.6293	0.4051	0.346
ρ_{mse} (modified reflectance)	0.1304	0.1193	0.6018	0.5851	0.4428	0.3508
ρ_{me} (modified reflectance)	0.1234	0.1104	0.5309	0.5189	0.3692	0.3033

Figure 5 shows the relationships between the modified reflectance of the three targets and incident angle when detection distances were changed in experiments. The subplots (a), (b), and (c) in the upside of Fig. 5 are the modified reflectance results estimated by the IW method, and the subplots (d), (e), and (f) below are modified reflectance results estimated by the PF method. As seen from Fig. 5, the black dashed lines represent the modified reflectance ρ_{mse} calculated from Eq. (16) based on the semi-ellipsoid model, while the gray solid lines represent the modified reflectance ρ_{me} calculated from Eq. (17) based on the ellipsoid model. The modified values are also displayed in the fifth and sixth rows of Table 3, respectively. It can be noted that the modified reflectance ρ_{mse} and ρ_{me} for the three targets are roughly distributed in a horizontal line, which means that the modified reflectances are approximately constant and can represent the average ability of material reflectance. The modified reflectance values of gray-cement concrete using the IW method are calculated to be 0.1304 ± 0.0340 using Eq. (16) and 0.1234 ± 0.0325 using Eq. (17), respectively. The modified reflectance of gray-cement concrete using PF method are calculated to be 0.1193 ± 0.0160 using Eq. (16) and 0.1104 ± 0.0161 using Eq. (17), respectively. From the values of StD, it can be seen that better results with the minimal error can be deduced by the PF method. It can also be deduced from the other two targets. And the modified reflectance estimated for red dull paper and glazed indoor tile calculated by PF method are 0.5850 ± 0.0441 and 0.3508 ± 0.0746 using Eq. (16) 0.5190 ± 0.0886 and 0.3031 ± 0.0982 using Eq. (17), respectively. The StD of the modified reflectance ρ_{mse} estimated for three targets are smaller than StD of ρ_{me}. In general words, the modified reflectance obtained by the PF method based on the semi-ellipsoid model has the minimal error.

As shown in Fig. 6, the two kinds of reflectance, which are the modified reflectance and the fitting reflectance, are estimated in a combined manner of two energy-estimation methods (IW and PF) and two modified reflection distribution models (EDR and SEDR). The combined manners are labeled on the x-coordinate. For example, IW-FSE means the

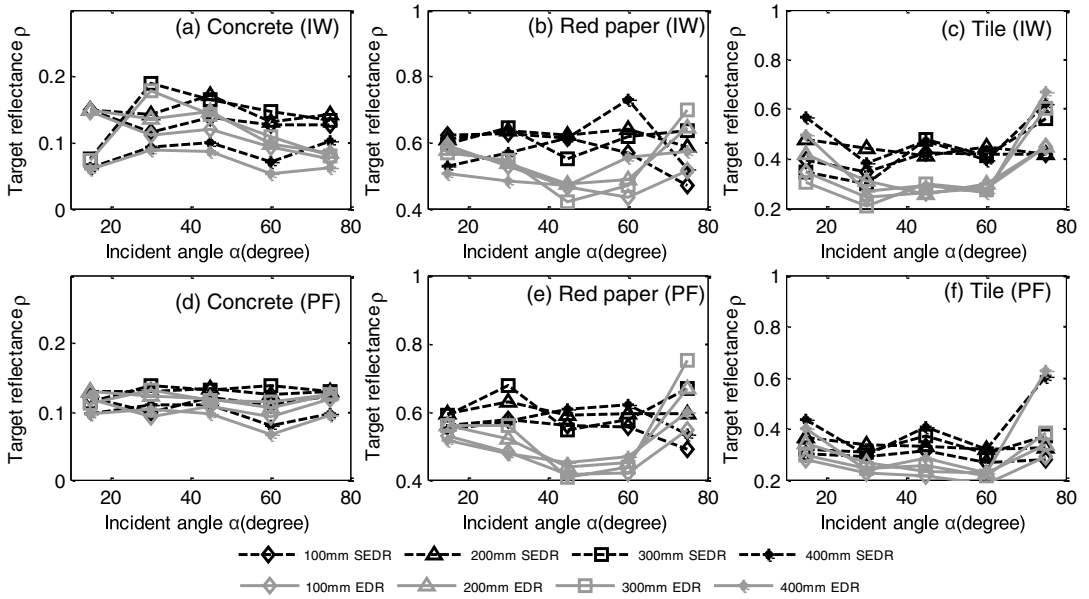

Fig. 5 Modified reflectance based on semi-ellipsoid model and ellipsoid model at different incident angles and detection distances.

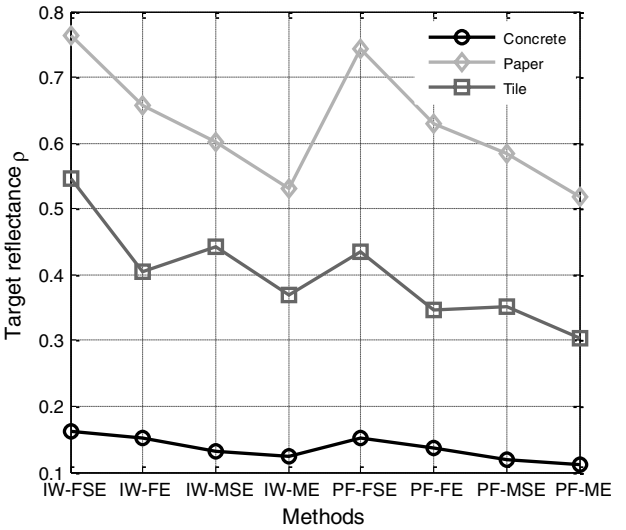

Fig. 6 Modified reflectance based on two energy-estimation methods and two empirical models.

fitting reflectance estimated using the IW method and SEDR, while the PF-ME means the modified reflectance estimated using the PF method and EDR. We can see that the eight results for each target display definite and potential links among each other. First, the reflectance values estimated from both IW and PF methods have a similar distribution trend, as shown in the first four reflectance data and the last four reflectance data in Fig. 6. Second, the reflectance values estimated from the IW method are bigger than those estimated from the PF method. This is because the energy of the received pulse using the IW-based method contains more noise than the energy of received pulse using the PF-based method. In summary, the modified reflectance can be used for reflectance estimation based on the PF method.

4.3.2 *Reflectance calibration*

No studies of the influences of composition and exposure on the infrared reflectance of gray-cement concrete were found in an extensive electronic search of engineering, physics, material science, and transportation literatures. However, we can calibrate and estimate the results according to the emissivity of the targets. Essentially, emissivity is the relative ability of a material's surface to emit energy as radiation. In general, the duller and blacker a material is, the closer its emissivity is to 1. The more reflective a material is, the lower its emissivity is. Most solid objects exhibit very low transmission of infrared energy; thus the majority of incident energy is either absorbed or reflected. It can be stated as follows:

$$100\% = \text{Emissivity} + \text{reflectivity}. \tag{18}$$

If emissivity increases, reflectance must decrease. For example, a plastic material with an emissivity of 0.92 has a reflectivity of 0.08. In this paper, the material was underlying in the infrared; tables of emissivity values in the infrared are only approximated values for real materials, which are provided in Refs. 23 and 24. A range of emissivity values are usually given for many materials whose emissivity can be affected by surface roughness or finish. The emissivity value of concrete, which has a rough surface and gray color, is 0.97, and the emissivity value of paper, which has a dull surface and red color, maybe 0.9, while the emissivity value of tile, which has a smooth surface and gray color, is 0.94. Thus, the approximated reflectance values are close to 3:10:6 for gray-cement concrete, red dull paper, and glazed indoor tile. This can provide a calibration standard for the modified reflectance. Here, we have obtained that the average 1064-nm reflectance of the gray-cement concrete was 11.93%; the average 1064-nm reflectance of the red dull paper was 58.51%; and the average 1064-nm reflectance of the brown glazed tile was 35.08%. Thus, modified reflectance is close to 1:5:3 for gray-cement concrete, red dull paper, and glazed indoor tile. It is clear that there is a definite link between the modified reflectance ratio and the reflectivity deduced by certain emissivity of the targets. This provides the credible basis for our results to some extent.

5 Conclusion

In this study, a full-waveform laser detection system was built to study the reflectance of three different targets, which are gray-cement concrete, red dull paper, and gray indoor tile. Based on this laser detection system, the returned waveforms of these three different objects were collected. The filtered waveforms were used to calculate the returned energy of these different targets at 1064 nm in the infrared band, and then the reflectance can be calculated with different models. The returned energy was calculated by two methods (IW method and PF method), and the results show that the echo pulse energy is inversely proportional to the square of the detection distance. Moreover, it has been indicated that the PF method is better than the IW method since the PF method can create the noise elimination effect. When the reflectance was calculated depending upon the Lambertian-based scattering light theory, the results are not consistent with physical reality. Thus, empirical models, which are the semi-ellipsoid model and the ellipsoid model, for non-Lambertian are put forward to recalculate the reflectance of the targets. The ratio of semiprincipal axes, SEDR of the semi-ellipsoid model, and EDR of the ellipsoid model could be used as the empirical factors to describe the degree of non-Lambertian-based material scattering, and the bigger values of SEDR and EDR reveal targets with more deviation from non-Lambertian. The modified reflectance shows that the semi-ellipsoid model is most applicable here and has a linear relationship with the fitting reflectance.

Acknowledgments

The research work is supported in part by the National Natural Science Foundation of China under Grant Nos. 61201316 and 61225006 and Specialized Research Fund for the Doctoral Program of Higher Education (No. 20121102120040).

References

1. R. Montes and C. Ureña, "An overview of BRDF models," LSI Technical Report, 2012-001, Department Lenguajes y Sistemas Informáticos, University of Granada, Granada, Spain (2012).
2. F.Y. Huang et al., "Influence of background radiation on space target detection in the long wave infrared range," *Opt. Eng.* **51**(8), 086402 (2012).
3. K. A. Herren and D. A. Gregory, "Bidirectional reflectance distribution function measurement of molecular contaminants in the ultraviolet, vacuum ultraviolet, and visible ranges," *Opt. Eng.* **46**(11), 113601 (2007).

4. G. Meister et al., "Investigation on the Torrance-Sparrow specular BRDF model," in *Geoscience and Remote Sensing Symp. Proc. IGARSS '98, Seattle, WA* Vol. 4, pp. 2095–2097 (1998).
5. Q. Z. Zhu and Z. M. Zhang, "Correlation of angle-resolved light scattering with the microfacet orientation of rough silicon surfaces," *Opt. Eng.* **44**(7), 073601 (2005).
6. R. L. Cook and K. E. Torrance, "A reflectance model for computer graphics," *Comput. Graph. Interact. Tech.* **15**(3), 307–316 (1981).
7. M. Oren and S. K. Nayar, "Generalization of Lambert's reflectance model," in *Proc. of ACM SIGGRAPH 94*, pp. 239–246 (1994).
8. W. Matusik, "A data-driven reflectance model," PhD Thesis, Massachusetts Institute of Technology (2003).
9. M. Minnaert, "The reciprocity principle in lunar photometry," *Astrophys. J.* **93**, 403–410 (1941).
10. B. T. Phong, "Illumination for computer generated pictures," *ACM Commun.* **18**(6), 311–317 (1975).
11. A. L. Yuille, "Lecture 10: the Lambertian reflectance model," 2012, http://www.learningace.com/doc/4381368/f934eff4c7f95a78485d792c5c108dfd/lecture10 (10 May 2013).
12. X. Liu, H. M. Tulldahl, and A. Axelssona, "An overview of the airborne bathymetric LiDAR reflectance data processing," *Proc. SPIE* **8286**, 828608 (2011).
13. S. Kaasalainen et al., "Analysis of incidence angle and distance effects on terrestrial laser scanner intensity: search for correction methods," *Remote Sens.* **3**(10), 2207–2221 (2011).
14. B. Höfle and N. Pfeifer, "Correction of laser scanning intensity data: data and model-driven approaches," *ISPRS J. Photogramm. Remote Sens.* **62**(6), 415–433 (2007).
15. W. Wagner, "Radiometric calibration of small-footprint full-waveform airborne laser scanner measurements: basic physical concept," *ISPRS J. Photogramm. Remote Sens.* **65**(6), 505–513 (2010).
16. P. F. McManamon, "Review of ladar: a historic, yet emerging, sensor technology with rich phenomenology," *Opt. Eng.* **51**(6), 060901 (2012).
17. J. S. Wei et al., "Experimental study on object reflection of imaging laser radar," in *Academic Int. Symp. on Optoelectronics and Microelectronics Technology*, Harbin, China, Vol. 2, pp. 179–182, IEEE (2011).
18. V. V. Alexander et al., "Surface roughness measurement of flat and curved machined metal parts using a near infrared super-continuum laser," *Opt. Eng.* **50**(11), 113602 (2011).
19. C. Mallet and F. Bretar, "Full-waveform topographic lidar: state-of-the-art," *ISPRS J. Photogramm. Remote Sens.* **64**(1), 1–16 (2009).
20. B. Jutzi and U. Stilla, "Laser pulse analysis for reconstruction and classification of urban objects," *ISPRS J. Photogramm. Remote Sens.* **XXXIV**(part3/W8), 151–156 (2003).
21. M. Kirchhof and B. Jutzi, "Iterative processing of laser scanning data by full waveform analysis," *ISPRS J. Photogramm. Remote Sens.* **63**(1), 99–114 (2007).
22. W. Wagner et al., "Gaussian decomposition and calibration of a novel small-footprint full-waveform digitising airborne laser scanner," *ISPRS J. Photogramm. Remote Sens.* **60**(2), 100–112 (2006).
23. Infrared Services Inc., "Emissivity Values for Common Materials," http://www.infrared-thermography.com/material-1.htm (22 July 2013).
24. Electronic Temperature Instruments Ltd., "Emissivity table," http://thermometer.co.uk/img/documents/emissivity_table.pdf (22 July 2013).

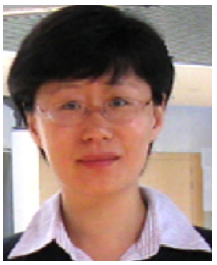

Xiaolu Li received her BS degree in electronic science and technology from Yanshan University, Qinhuangdao, China, in 2003 and her PhD degree in physical electronics from Beihang University, Beijing, China, in 2009. From 2007 to 2009, she was as a visiting scholar with the Department of Electrical and Computer Engineering, Johns Hopkins University, Baltimore, Maryland. Her research interests include fiber optics and LiDAR systems.

Lian Ma received her BSc degree in measurement and control technology and instrument from University of Science and Technology Beijing, China, in 2012. She is currently a master candidate in the School of Instrument Science and Opto-Electronic Engineering, Beihang University, Beijing, China. Her current research focuses on full-waveform LiDAR system and data process.

Lijun Xu received his BSc, MEng, and PhD degrees in electrical engineering and instrumentation from Tianjin University, Tianjin, China, in 1990, 1993, and 1996, respectively. From 1997 to 2001, he was an associate professor with the School of Electrical Engineering and Automation, Tianjin University. From January 2002 to December 2004, he was a research fellow with the University of Greenwich at Medway, Chatham, United Kingdom and the University of Kent, Canterbury, United Kingdom. From December 2004 to April 2006, he was a higher scientific officer with the Department of Physics, Institute of Cancer Research, University of London, London, United Kingdom. He is currently a professor with the School of Instrument Science and Opto-Electronic Engineering, Beihang University, Beijing, China. His current research interests include digital imaging and dynamic process monitoring.